PAPER

Check for updates

Lattice-distorted lithiation behavior of a square phase Janus MoSSe monolayer for electrode applications†

Xin Tang,[a] Han Ye, [ID] *[a] Wenjun Liu, [ID] [a] Yumin Liu, [ID] [a] Zhenlin Guo[b] and Mingchao Wang [ID] *[cd]

Janus transition metal dichalcogenides with unique physical properties have recently attracted increasing research interest for their energy and catalytic applications. In this paper, we investigate the lithiation behavior of a square phase Janus MoSSe monolayer (1S-MoSSe) using first-principles calculations. Computational results show that a single Li atom energetically prefers to adsorb on the central site of the octagonal ring (O site) and on the S-layer side of 1S-MoSSe. The predicted energy barriers for Li diffusion are surface dependent and in the range of 0.33 to 0.51 eV, indicating the acceptable Li migration kinetics on 1S-MoSSe in comparison with other 2D TMD materials. Further thermodynamic analysis demonstrates that Li adsorption on 1S-MoSSe is energetically stable up to a Li concentration of $x = 1.0$, above which the lithiation process becomes unstable with a negative charging potential. Phonon calculations also confirm that Li adsorption ($0.25 \leq x \leq 0.75$) results in the lattice distortion of 1S-MoSSe in order to suppress the structural instability of the lithiated monolayer 1S-Li$_x$MoSSe with imaginary phonon frequencies. The less symmetric nature of 1S-MoSSe is believed to destabilize Li adsorption at much smaller x than 1H-MoSSe does, regardless of the higher dipole moment of 1S-MoSSe. This computational study provides a fundamental understanding of the electrochemical performance of 1S-MoSSe, as well as useful insight into the material design of Janus TMD anodes for Li-ion batteries.

1. Introduction

Layer-structured materials with two-dimensional (2D) layer components have attracted wide research interest for their energy applications in alkali metal batteries owing to their unique physical properties (*i.e.* large surface area and fast ion transport).[1-3] Among various 2D-based materials, graphene and transition metal dichalcogenide (TMD) based materials have been widely studied as potential electrodes for Li-ion batteries (LIBs).[3-5] For example, graphite has been used as a commercial anode in LIBs due to its excellent electrical conductivity and good stability.[6,7] However, the graphite anode suffers from a low capacity of 372 mA h g^{-1}, which hardly satisfies the current energy demand for electrified vehicles and grid energy storage.[8,9] As for TMD-based materials, although certain TMD candidates such as MoS$_2$ exhibit excellent specific capacity as high as 554 mA h g^{-1},[10] they still suffer from low electrical conductivities, as well as sluggish ion diffusion within the interlayer spacings.[4,5,11] It is therefore urgently necessary to enhance the battery performance of layered material electrodes with excellent thermodynamic and kinetic stabilities.

Recently, various material design strategies have been proposed for improving the electrochemical properties of 2D-based electrodes for LIBs. For instance, layered materials with heterostructures (*i.e.* graphene/MoS$_2$ (ref. 12 and 13)) or expanded interlayer spacings[14-16] enable the acceleration of Li intercalation kinetics, while it is compensated with capacity fading and cycling stability due to the weakened interaction between the layer structures and Li ions. In the extreme case of interlayer expansion, some 2D materials, including graphene and MoS$_2$, become thermodynamically unstable upon Li adsorption, resulting in the irreversible formation of Li metal clusters.[17-19] To overcome such a limitation, surface defects in 2D layers have been demonstrated as an effective way to enhance the thermodynamic stability of both graphene and TMD monolayers, contributed by increased charge transfer.[20-23] Unfortunately, such a defect engineering method is highly

[a]*State Key Laboratory of Information Photonics and Optical Communications, Beijing University of Posts and Telecommunications, Beijing 100876, China. E-mail: Han_ye@bupt.edu.cn*

[b]*Mechanics Division, Beijing Computational Science Research Center, Beijing 100193, China*

[c]*Department of Materials Science and Engineering, Monash University, Clayton, VIC 3800, Australia. E-mail: mingchao.wang@monash.edu*

[d]*Centre for Theoretical and Computational Molecular Science, Australian Institute for Bioengineering and Nanotechnology, The University of Queensland, St Lucia, QLD 4072, Australia*

† Electronic supplementary information (ESI) available: Figures. See DOI: 10.1039/d1na00112d

limited by its uncontrollable synthesis procedure and undesired mechanical failure upon lithiation.

In addition to defect engineering, synthesizing novel phases of regular graphene and TMD structures serves as an alternative way to improve their electrochemical performance for LIBs. For example, some allotropes of graphene, such as phagraphene (defected graphene with 5- to 7-membered rings)[24,25] and graphdiyne,[17,26,27] exhibit both excellent ion mobility and high specific capacity as promising anodes for LIBs. A square phase allotrope of MoS_2 is also observed near the grain boundary of H-phase MoS_2,[28–30] and is predicted to possess a theoretical capacity of 670 mA h g^{-1}.[31] Compared with regular TMDs, recent experiments have successfully fabricated a new class of TMD structures called Janus TMDs (*i.e.* MoSSe), with controlled sulfurization of their one-side atoms.[32–34] The intrinsic dipole moment of H-phase (H-) Janus MoSSe promotes Li adsorption, leading to an improved thermodynamic stability.[35] Different from square phase TMDs, there is lack of intensive investigation on the electrochemical behavior of square phase Janus TMDs, regardless of recent theoretical studies of their catalytic applications.[36–38]

With the above in mind, we carry out a systematic study of the Li adsorption behavior of a square phase Janus MoSSe monolayer (1S-MoSSe) as a LIB anode using first-principles calculations. Structural, energetic and electrochemical properties of 1S-MoSSe upon lithiation are predicted respectively. It is found that 1S-MoSSe has more energetically stable binding sites than some other TMD-based monolayers. Different Li migration pathways and kinetics are analyzed as well. Finally, we estimate the thermodynamic stability, as well as open cell voltage and Li storage capacity, of lithiated 1S-MoSSe at the Li concentration of x, denoted as 1S-Li_xMoSSe. Phonon calculations demonstrate that Li adsorption results in the structural instability of Li_x-MoSSe, and is further suppressed by local lattice distortion. In addition, 1S-MoSSe has a maximum Li concentration of $x = 1.0$ (129.47 mA h g^{-1}), above which Li adsorption becomes unstable associated with a negative charging voltage.

2. Computational methods

All density functional theory (DFT) calculations are conducted using the Vienna *ab initio* simulation package (VASP) code.[39] The electron core-valence and exchange–correlation interactions are described by projector augmented plane wave (PAW) pseudopotentials[40] and the Perdew–Burke–Ernzerhof (PBE) functional,[41] respectively. We select a plane-wave based kinetic energy cutoff of 600 eV, and the $5 \times 5 \times 1$ Monkhorst–Pack[42] k-point mesh for sampling the Brillouin zones of Janus structures. The thickness of vacuum spacing is set as 18 Å to avoid the interaction between the Janus monolayer and its images. Atomic structures are optimized until the force and energy of each atom are smaller than 0.02 eV $Å^{-1}$ and 10^{-6} eV, respectively. Grimme's energy correction method (DFT-D3) is employed to correctly account for long-range dispersion interactions.[43] Dipole correction is also considered here along the z axis to eliminate any spurious interaction between Janus monolayers.

The Bader charge analysis[44,45] is conducted to analyze the charge transfer between Li ions and the MoSSe monolayer. The minimum energy paths of Li ion migration are identified through the climbing image nudged elastic band (CI-NEB) method.[46] In order to assess the dynamic stability of Janus monolayers upon Li adsorption, their vibrational properties are obtained from phonon dispersion calculations based on density functional perturbation theory. The force constant matrix is constructed from the $3 \times 3 \times 1$ supercell in the PHONOPY package.[47] The adsorption energy per Li atom (E_{ads}^{atom}) is defined as:

$$E_{ads}^{atom} = \frac{E_{MoSSe-Li} - nE_{Li} - E_{MoSSe}}{n}, \qquad (1)$$

where $E_{MoSSe-Li}$ and E_{MoSSe} are the total energies of the 1S-MoSSe supercell with/without Li adsorption; n is the total number of adsorbed Li atoms; E_{Li} is the energy of an isolated Li atom. The formation energy (E_f^{atom}) per Li atom is similarly defined as:

$$E_f^{atom} = \frac{E_{MoSSe-Li} - n\mu_{Li} - E_{MoSSe}}{n}, \qquad (2)$$

where μ_{Li} is the energy of a Li atom in the Li bcc crystal. The adsorption and formation energies per MoSSe unit cell (E_{ads}^{unit} and E_f^{unit}) can be evaluated according to their per Li atom values as:

$$E_{ads}^{unit} = \frac{n}{N}E_{ads}^{atom}, \quad E_f^{unit} = \frac{n}{N}E_f^{atom} \qquad (3)$$

where N is the total unit number of Mo atoms in the MoSSe supercell, and the Li adsorption concentration x can be expressed as $x = n/N$. Open cell voltage (OCV) is another important electrochemical characteristic of electrodes and is defined by:[48]

$$\begin{aligned} OCV &\approx \frac{E_{Li_{x_1}MoSSe} - E_{Li_{x_2}MoSSe} + (n_2 - n_1)\mu_{Li}}{(n_2 - n_1)e} \\ &= \frac{E_f^{unit}(Li_{x_1}MoSSe) - E_f^{unit}(Li_{x_2}MoSSe)}{(x_2 - x_1)e}, \end{aligned} \qquad (4)$$

where $E_{Li_{x_1}MoSSe}$ and $E_{Li_{x_2}MoSSe}$ are the total energies of the lithiated structures Li_xMoSSe, and $E_f^{unit}(Li_{x_1}MoSSe)$ and $E_f^{unit}(Li_{x_2}$-MoSSe) are the formation energies per MoSSe unit cell, at adjacent Li concentrations of x_1 and x_2.

3. Results and discussion

3.1 Structural and electronic properties of 1S-MoSSe

We first evaluate the fundamental properties of the 1S-MoSSe monolayer. Fig. 1(a and b) exhibits the relaxed 2×2 supercell of 1S-MoSSe consisting of alternating square and octagonal rings. The lattice constant of the primitive cell is 6.421 Å, with a thickness of 3.243 Å. As shown in Table 1, the nearest Mo–S (2.449 Å) and Mo–Se (2.587 Å) bonds in the square ring are both longer than those in the octagonal ring (2.393 Å and 2.484 Å, respectively), which is well consistent with previous computational results.[36,37] 1S-MoSSe has a lattice constant and thickness that are between those of the 1S-MoS_2 and 1S-$MoSe_2$ monolayers, while the trend of Mo–S and Mo–Se bond lengths among
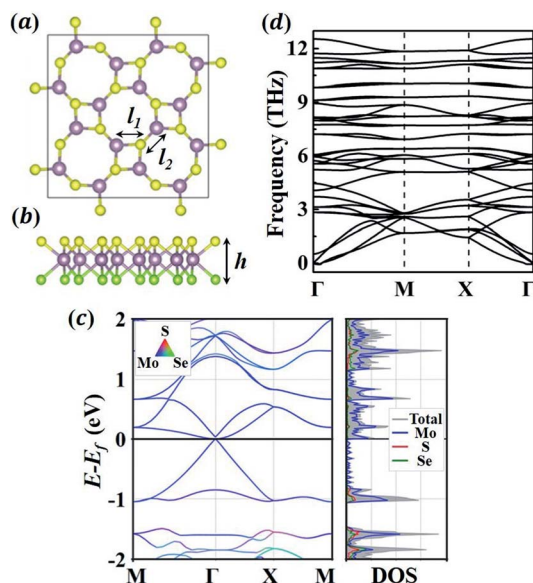
Fig. 1 (a) Top view and (b) front view of the relaxed atomic structure of 1S-MoSSe. Mo, S, and Se atoms are represented by purple, yellow and green colors, respectively. (c) The electronic band structures and density of states (DOS) of 1S-MoSSe. (d) The phonon dispersion curves of 1S-MoSSe.

Table 1 The structural parameters of the 1S-MoSSe primitive cell. The lattice constant of the primitive cell (a, b); bond lengths marked in the structure (l), l_1 is the bond length in the square ring and l_2 is the bond length in the octagonal ring; layer height (h)

|	$a = b$ (Å)	l(Mo–S) (Å)	l(Mo–Se) (Å)	h (Å)
MoSSe	6.421	l_1: 2.449	l_1: 2.587	3.243
	6.474 (ref. 36)	l_2: 2.393	l_2: 2.484	
MoS$_2$	6.289	l_1: 2.451		3.136
	6.336 (ref. 50)	l_2: 2.375		
MoSe$_2$	6.559		l_1: 2.584	3.348
	6.613 (ref. 50)		l_2: 2.500	

these 3 monolayers is unobvious. Owing to the structural asymmetry, 1S-MoSSe has a dipole moment of 2.99 Debye along its thickness direction, which is larger than that of the 1H-MoSSe monolayer (1.61 Debye). The effect of dipole moment on its Li adsorption behavior will be discussed later.

Fig. 1(c) characterization of the electronic properties of 1S-MoSSe. Different from 1H-MoS$_2$ and 1H-MoSe$_2$,[49] 1S-MoSSe behaves as a semi-metal with the valence band maximum and conduction band minimum crossing each other at the Fermi-level, which has also been observed in other square-phase TMD monolayers.[31,50] In addition, the phonon dispersion curves (see Fig. 1(d)) of 1S-MoSSe are predicted to determine its intrinsic structural stability. The absence of imaginary frequencies around the Γ point in the reciprocal space confirms that 1S-MoSSe is dynamically stable. As a result, the robustness of 1S-MoSSe guarantees it as an anode candidate for LIBs.

3.2 Energetic and electronic properties of Li adsorption on 1S-MoSSe

To understand the lithiation behavior of 1S-MoSSe, we then explore its potential binding sites for isolated Li atom adsorption. The 2×2 supercell of 1S-MoSSe is adopted here. To identify the most stable site for Li adsorption, three possible sites on each side of 1S-MoSSe are considered, including the O site: the central site of the octagonal ring; the T_{Mo} site: the top site of Mo; and the square site: the central site of the square ring, as presented in Fig. 2(a and b). According to the definition of adsorption energy per Li atom (E_{ads}^{atom}) in eqn (1), the more negative value of E_{ads}^{atom} the system possesses, the more energetically favorable the binding site is. Fig. 2(c) demonstrates that the O site on both sides of 1S-MoSSe has the lowest value of E_{ads}^{atom}, indicating it as the most energetically favorable site for Li adsorption followed by T_{Mo} and square sites. Fig. 2(c) also shows that these binding sites on the S-layer side have a lower E_{ads}^{atom} than those on the Se-layer side, which can result in asymmetric Li adsorption. In addition, all 3 binding sites on 1S-MoSSe are more energetically stable than those on 1S-MoS$_2$ and 1S-MoSe$_2$. Such a higher binding strength of 1S-MoSSe can be attributed to the existence of its dipole moment, which facilitates Li adsorption by an intrinsic electric field.[35]

To further understand the asymmetric Li adsorption behavior of 1S-MoSSe, we calculate the electronic properties of 1S-MoSSe with a single Li atom adsorbed on the O sites of both sides, labeled as 1S-MoSSe_S + Li and 1S-MoSSe_Se + Li, respectively. Fig. 3(a and b) show that both adsorption systems are still semi-metallic with zero band gap at the Fermi level. The corresponding charge transfer is analyzed on the basis of charge density difference (see Fig. 3(c)). It is shown that charge accumulation occurs in 1S-MoSSe, whereas charge depletion occurs
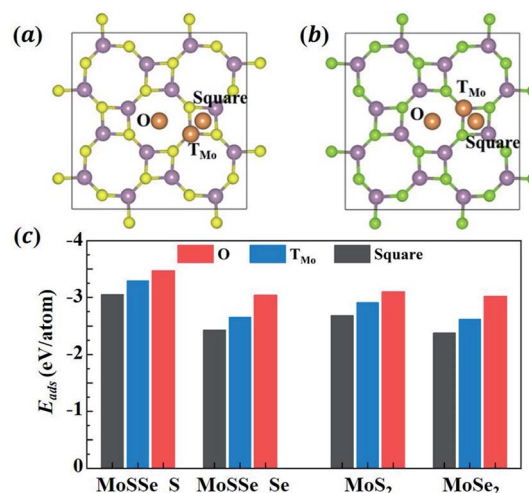
Fig. 2 (a and b) The atomic structures of the 2×2 supercell of 1S-MoSSe adsorbing a single Li atom at different sites (O, T_{Mo} and square sites) on (a) S-layer and (b) Se-layer sides. Li, Mo, S and Se atoms are represented by orange, purple, yellow and green colors, respectively. (c) The adsorption energy of a single Li atom adsorbed on different sites of the 2×2 supercell of 1S-MoSSe, 1S-MoS$_2$ and 1S-MoSe$_2$.
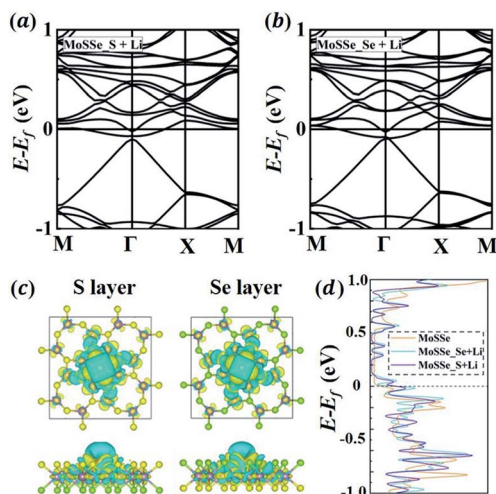
Fig. 3 (a and b) The band structures of 1S-MoSSe adsorbing a single Li atom on (a) S-layer and (b) Se-layer sides, denoted as 1S-MoSSe_S + Li and 1S-MoSSe_Se + Li, respectively. (c) The charge density difference of 1S-MoSSe_S + Li and 1S-MoSSe_Se + Li systems. Cyan and yellow iso-surfaces denote charge depletion and accumulation. (d) Electronic density of states (DOS) of 1S-MoSSe, 1S-MoSSe_S + Li and 1S-MoSSe_Se + Li.

on the Li atom. Bader charge calculations confirm that more electrons (0.87 e) transfer from the Li atom to the S-layer side than to the Se-layer side (0.84 e), which supports the ionic nature of Li adsorption. The electronic DOS curves of 1S-MoSSe before and after Li adsorption are given in Fig. 3(d). Different from the pristine 1S-MoSSe, 1S-MoSSe_S + Li and 1S-MoSSe_Se + Li systems exhibit narrower DOS peaks near the Fermi level,

and the DOS peaks of 1S-MoSSe_S + Li are slightly closer to the Fermi level compared to those of 1S-MoSSe_Se + Li. This also represents the higher adsorption strength of 1S-MoSSe_S + Li than that of 1S-MoSSe_Se + Li. Based on this consideration, Li adsorption should start from the S-layer side, accompanied by the gradual adsorption of more Li on both sides upon lithiation. The electronic band structure and DOS of the system with Li adsorbed on T_{Mo} and square sites are illustrated in Fig. S1 in the ESI.†

3.3 Kinetics of Li migration on 1S-MoSSe

In addition to the energetics of Li adsorption, here, we study the kinetics of Li migration on 1S-MoSSe. To determine the optimal migration path and the corresponding energy barrier, we consider three Li diffusion pathways on 1S-MoSSe (see Fig. 4(a–c)): (1) a Li atom diffuses between two nearest O sites; (2) a Li atom diffuses from an O site to the nearest square site; (3) a Li atom diffuses from an O site on the S-layer side to the neighboring O site on the Se-layer side. The minimum energy paths (MEPs) and corresponding diffusion barriers are presented in Fig. 4(d and e). For route 1 on both sides of 1S-MoSSe, the corresponding MEPs form zigzag shaped curves which span across another energy minimum site between 2 nearest O sites. Owing to the asymmetry of 1S-MoSSe, such an energy minimum site is different from the T_{Mo} site (see Fig. 2(a and b)), which results in the asymmetric shape of MEPs. Between the different sides of 1S-MoSSe for route 1, the calculated energy barrier on the Se-layer side is 0.51 eV higher than that on the S-layer side of 0.33 eV, which is interestingly in contrast to the difference between their adsorption energies on different binding sites.
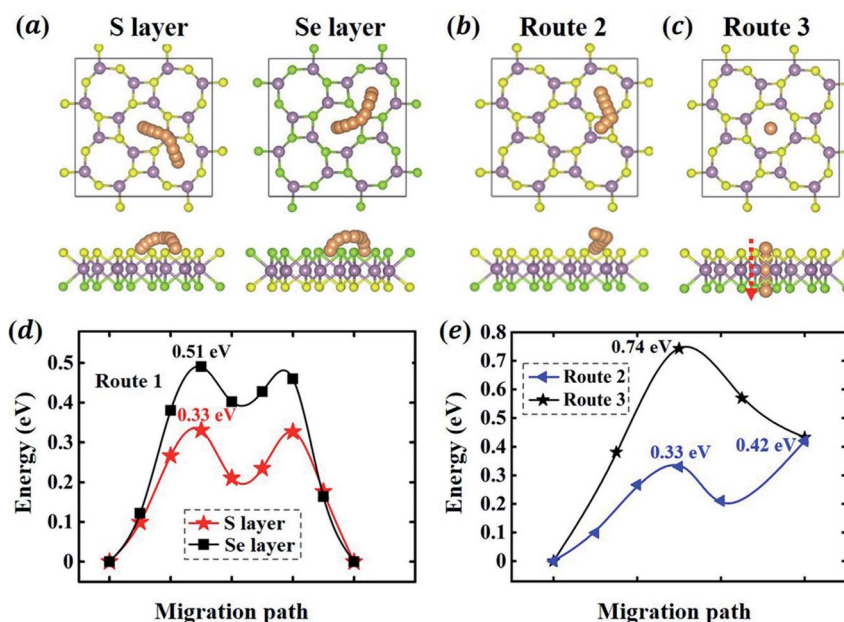
Fig. 4 Atomistic representation (a–c) and calculated minimum energy paths (d and e) of 3 different migration routes on 1S-MoSSe, which include route 1: a Li atom migrates between two nearest O sites on the S- and Se-layer sides, respectively; route 2: a Li atom migrates from the O site to the nearest square site on the S-layer side; route 3: a Li atom migrates from an O site on the S-layer side to the neighboring O site on the Se-layer side.

Since the S-layer side has a much lower energy barrier for route 1, routes 2 and 3 are only considered on the S-layer side. The diffusion barrier for route 2 is 0.42 eV, and the T_{Mo} site is thermodynamically unstable and will migrate to a nearby energy minimum site under certain perturbations. The higher diffusion barrier for route 2 (0.42 eV) than that for route 1 (0.33 eV) results from the thermodynamical instability of square site. As for route 3, however, it requires much higher energy (0.74 eV) to migrate across the Janus monolayer. The energy barriers for surface migration routes on 1S-MoSSe (0.33–0.51 eV) are a little bit higher than those on 1H-MoSSe (0.24–0.29 eV)[35] as well as 1H-MoS$_2$ (0.21 eV) and 1H-MoSe$_2$ (0.225 eV).[18] As a result, 1S-MoSSe may have slower but comparable Li migration kinetics according to the Arrhenius relationship.

3.4 Electrochemical properties of 1S-MoSSe upon lithiation

Finally, we calculate the thermodynamic properties of the lithiated Janus MoSSe monolayer (1S-Li$_x$MoSSe) at a Li concentration of $x = 0.125$–1.0 with an increment of $\Delta x = 0.125$. As discussed in the previous section, Li prefers to adsorb on the S-layer side rather than the Se-layer side. In order to determine the most energetically stable configurations at different values of x, Li atoms are placed preferentially on the O sites of the S-layer side when $x \leq 0.5$. As for $0.5 < x \leq 1$, the subsequent Li ions are randomly adsorbed on the O sites of the Se-layer side. Different adsorption configurations with the same Li concentration are considered. Fig. 5(a) and (c) show the adsorption energy per atom and per unit of different 1S-Li$_x$MoSSe configurations. All the negative adsorption energies imply that the process of Li adsorption on 1S-MoSSe is thermodynamically stable, but such a lithiation process gradually becomes more difficult, associated with the increase of E_{ads}^{atom} (Fig. 5(a)). It

should also be noted that E_{ads}^{atom} is much lower than the cohesive energy of the Li bcc crystal (−1.99 eV per atom) up to $x = 1.0$, indicating that Li adsorption on 1S-MoSSe is more energetically favorable than Li clustering. This is also consistent with all the negative values of formation energy in Fig. 5(b) and (d), and the charging/discharging process in such a concentration range is thermodynamically reversible without Li plating.

In addition to the thermodynamic analysis of 1S-Li$_x$MoSSe, we further perform phonon dispersion calculations to check the structural stability of 1S-Li$_x$MoSSe. As shown in Fig. 6(a–c), large negative frequencies occur at M and X points in the reciprocal space within the concentration range of $0 < x < 1$. These imaginary frequencies normally represent a dynamically unstable configuration (see Fig. 7(a–c)). After checking the corresponding eigenvectors of imaginary frequencies, minor structural distortion is introduced into 1S-Li$_x$MoSSe to find their stable configurations after relaxation. Fig. 7(d–f) shows that lattice distortion further stabilizes 1S-Li$_x$MoSSe with lower adsorption energy. Meanwhile, the phonon dispersion curves of distorted configurations in Fig. 6(d–f) also confirm the improvement of their structural stability. The updated high symmetric points for distorted configurations are shown in Fig. S2 (see the ESI†). With the increase of x, adsorbing more Li atoms can stabilize 1S-Li$_x$MoSSe at $x = 1.0$ (Fig. 6(g)) without imaginary frequencies at M and X points. It should be noted that the very small imaginary frequencies observed in Fig. 6(d–g) may result from numerical errors in phonon calculations.[51] Similar structural instability (imaginary frequencies) has also been found in other TMDs.[52–55] Different from the lattice distortion of 1S-Li$_x$MoSSe, the remarkable H to T phase transition of these TMDs suppresses their structural instability upon ion adsorption. Such a significant structural change induced by phase transition may trigger the
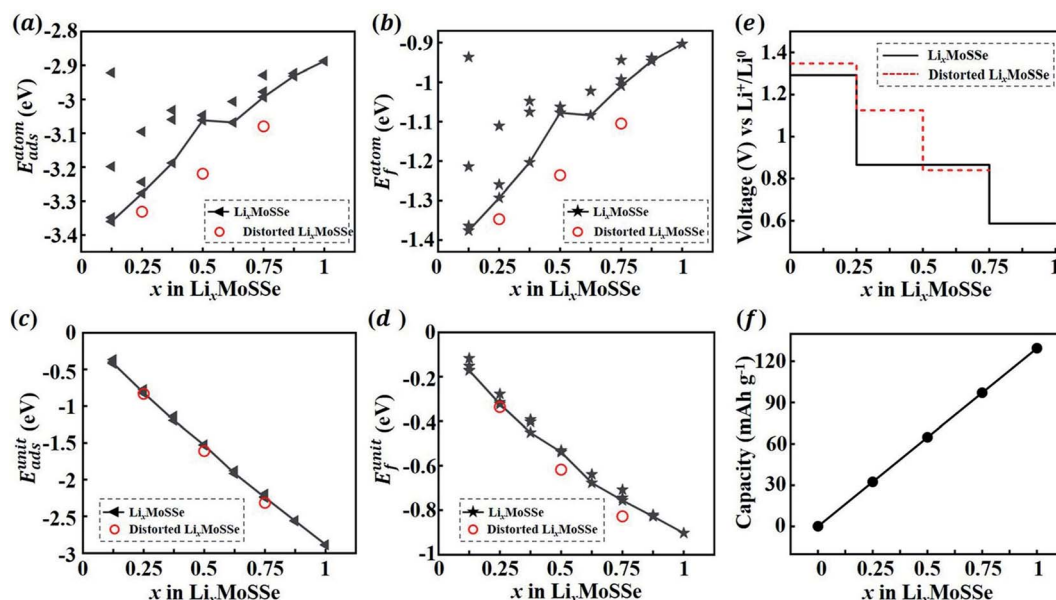
Fig. 5 Adsorption and formation energies per atom (a and c) and per unit cell (b and d) of 1S-Li$_x$MoSSe with respect to Li concentration x. Open cell voltage (OCV) profile (e) and specific capacity (f) as a function of x. The red circles in (a–d) and dashed line in (e) represent the energies and OCV of lattice distorted 1S-Li$_x$MoSSe, respectively.
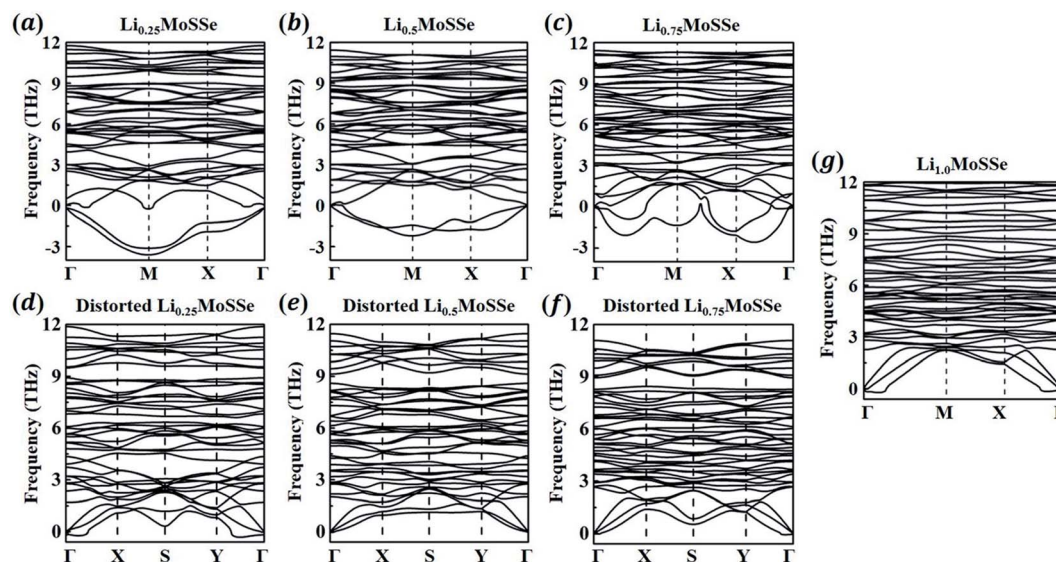
Fig. 6 Phonon dispersion curves of 1S-Li$_x$MoSSe without (a–c and g) and with (d–f) lattice distortion perturbation at a Li concentration of x = 0.25–1.0.

structural failure of these layered anodes, causing the degradation of battery performance.

Based on the calculated formation energies of 1S-Li$_x$MoSSe, we predict the open cell voltage (OCV) profile as a function of Li concentration. Fig. 5(e) shows that lattice distortion increases the initial OCV to ~1.35 V and then drops gradually to 0.59 V with the increase of Li adsorption. When x is larger than 1.0,

E_f^{unit} gets increased, and the evaluated negative charge potential according to eqn (4) indicates the initiation of an unstable charging process. Therefore, 1S-MoSSe has a maximum Li concentration of $x \sim 1.0$, while some TMD monolayers fail to stably adsorb Li atoms at extremely low x owing to the higher adsorption energy than the cohesive energy of the Li bcc crystal.[18] However, such a maximum concentration as well as
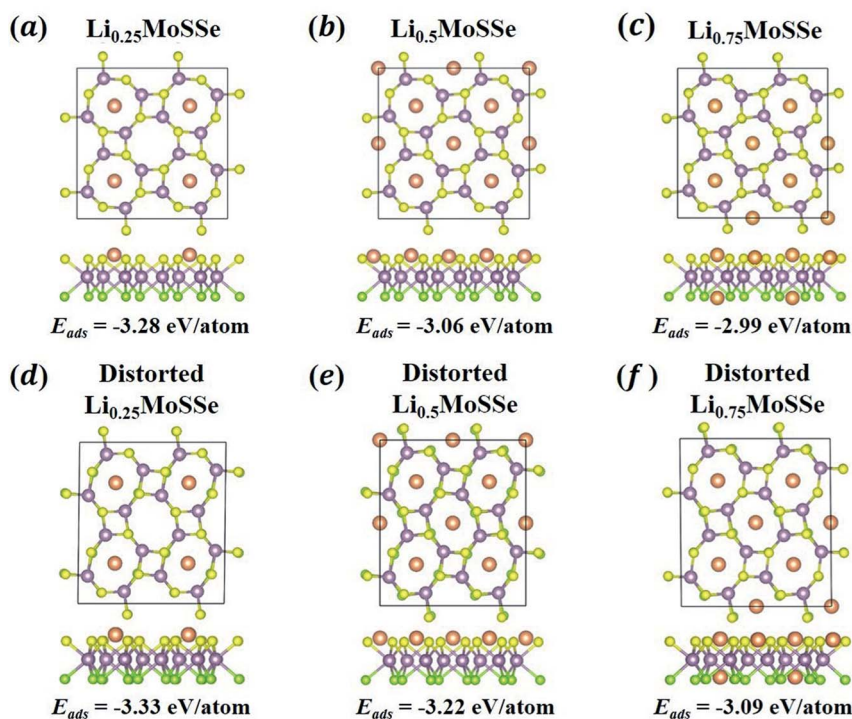

Fig. 7 The atomic configurations and adsorption energies of 1S-Li$_x$MoSSe without (a–c) and with (d–f) lattice distortion perturbation at a Li concentration of x = 0.25, 0.5 and 0.75.

the corresponding specific capacity (Fig. 5(f)) is still lower than those of 1S-MoS$_2$ (ref. 31) and 1H-MoSSe.[35] Such a capacity difference may be due to the fact that the less symmetric structure of 1S-MoSSe causes the unstable charging process at lower Li concentration. In addition, electronic DOS calculations (see Fig. S3 in the ESI†) show that 1S-Li$_x$MoSSe remains metallic and still has good electronic conductivity upon Li adsorption.

4. Conclusions

In summary, we conduct DFT calculations to investigate the structural, thermodynamic and electrochemical behaviors of a square phase Janus MoSSe monolayer (1S-MoSSe) for LIB anode applications. Computational results show that Li adsorption is most energetically stable at O sites on both sides of 1S-MoSSe, followed by the T$_{Mo}$ site and square site. The analysis of Li diffusion kinetics demonstrates that 1S-MoSSe possesses an acceptable surface Li mobility with an energy barrier in the range of 0.33 to 0.51 eV. Such Li migration behavior is also surface dependent and has faster diffusion kinetics on the S-layer side than on the Se-layer side. Energetic calculations of the charging (lithiation) process reveal that Li adsorption on 1S-MoSSe is thermodynamically stable and free of irreversible Li plating up to a Li concentration of $x = 1.0$, above which the lithiation process becomes unstable with a negative charging potential. Phonon calculations also exhibit that more Li adsorption ($0.25 \leq x \leq 0.75$) can trigger the structural instability of the lithiated monolayer, 1S-Li$_x$MoSSe, and be further suppressed by the lattice distortion of ring structures. Overall, 1S-MoSSe exhibits much better lithiation stability and capacitive behavior than other 2D TMD monolayers (i.e. 1H-MoS$_2$ and 1H-MoSe$_2$). However, the less symmetric nature of 1S-MoSSe is believed to destabilize Li adsorption at much smaller x than 1H-MoSSe does. This comprehensive study can provide fundamental insight into not only the electrochemical performance of other Janus TMD monolayers, but also the optimal design of high-performance TMD-based anodes for LIBs.

Author contributions

XT – methodology, formal analysis, writing – original draft; HY – conceptualization, supervision, funding acquisition; WL – writing – review and editing; YL – supervision, writing – review and editing; ZG – writing – review and editing; MW – conceptualization, writing – original draft.

Conflicts of interest

There are no conflicts to declare.

Acknowledgements

References

1 L. Peng, Y. Zhu, D. Chen, R. S. Ruoff and G. Yu, Two-Dimensional Materials for Beyond-Lithium-Ion Batteries, *Adv. Energy Mater.*, 2016, **6**, 1600025.

2 Y. Xue, Q. Zhang, W. Wang, H. Cao, Q. Yang and L. Fu, Opening Two-Dimensional Materials for Energy Conversion and Storage: A Concept, *Adv. Energy Mater.*, 2017, **7**, 1602684.

3 L. Ma, J. Wu, G. Zhu, Y. H. Lv, Y. Zhang and H. Pang, Recent Advances in Two-Dimensional Materials for Alkali Metal Anodes, *J. Mater. Chem. A*, 2021, **9**, 5232–5257.

4 B. Chen, D. Chao, E. Liu, M. Jaroniec, N. Zhao and S.-Z. Qiao, Transition Metal Dichalcogenides for Alkali Metal Ion Batteries: Engineering Strategies at the Atomic Level, *Energy Environ. Sci.*, 2020, **13**, 1096–1131.

5 Q. Yun, L. Li, Z. Hu, Q. Lu, B. Chen and H. Zhang, Layered Transition Metal Dichalcogenide-Based Nanomaterials for Electrochemical Energy Storage, *Adv. Mater.*, 2020, **32**, 1903826.

6 K. Persson, V. A. Sethuraman, L. J. Hardwick, Y. Hinuma, Y. S. Meng, A. van der Ven, V. Srinivasan, R. Kostecki and G. Ceder, Lithium Diffusion in Graphitic Carbon, *J. Phys. Chem. Lett.*, 2010, **1**, 1176–1180.

7 J. Billaud, F. Bouville, T. Magrini, C. Villevieille and A. R. Studart, Magnetically Aligned Graphite Electrodes for High-Rate Performance Li-Ion Batteries, *Nat. Energy*, 2016, **1**, 16097.

8 M. Winter, J. O. Besenhard, M. E. Spahr and P. Novák, Insertion Electrode Materials for Rechargeable Lithium Batteries, *Adv. Mater.*, 1998, **10**, 725–763.

9 S. W. Lee, N. Yabuuchi, B. M. Gallant, S. Chen, B.-S. Kim, P. T. Hammond and Y. Shao-Horn, High-Power Lithium Batteries from Functionalized Carbon-Nanotube Electrodes, *Nat. Nanotechnol.*, 2010, **5**, 531–537.

10 L. Wang, Y. Ma, M. Yang and Y. Qi, Hierarchical Hollow MoS$_2$ Nanospheres with Enhanced Electrochemical Properties Used as An Electrode in Supercapacitor, *Electrochim. Acta*, 2015, **186**, 391–396.

11 X. Sun, P. Bonnick and L. F. Nazar, Layered TiS$_2$ Positive Electrode for Mg Batteries, *ACS Energy Lett.*, 2016, **1**, 297–301.

12 K. Chang and W. Chen, L-Cysteine-Assisted Synthesis of Layered MoS$_2$/Graphene Composites with Excellent Electrochemical Performances for Lithium Ion Batteries, *ACS Nano*, 2011, **5**, 4720–4728.

13 K. Xu, N. Liao, M. Zhang and W. Xue, Atomic-Scale Investigation of Enhanced Lithium, Sodium and Magnesium Storage Performance from Defects in MoS$_2$/Graphene Heterostructures, *Nanoscale*, 2020, **12**, 7098–7108.

14 J. Shuai, H. D. Yoo, Y. Liang, Y. Li, Y. Yao and L. C. Grabow, Density Functional Theory Study of Li, Na, and Mg Intercalation and Diffusion in MoS$_2$ with Controlled Interlayer Spacing, *Mater. Res. Express*, 2016, **3**, 064001.

15 Y. Meng, Y. Zhao, D. Wang, D. Yang, Y. Gao, R. Lian, G. Chen and Y. Wei, Fast Li$^+$ Diffusion in Interlayer-Expanded

Vanadium Disulfide Nanosheets for Li$^+$/Mg^{2+} Hybrid-Ion Batteries, *J. Mater. Chem. A*, 2018, **6**, 5782–5788.

16 Y. Li, Y. Lu, P. Adelhelm, M.-M. Titirici and Y.-S. Hu, Intercalation Chemistry of Graphite: Alkali Metal Ions and Beyond, *Chem. Soc. Rev.*, 2019, **48**, 4655–4687.

17 C. Sun and D. J. Searles, Lithium Storage on Graphdiyne Predicted by DFT Calculations, *J. Phys. Chem. C*, 2012, **116**, 26222–26226.

18 D. Wang, L.-M. Liu, S.-J. Zhao, Z.-Y. Hu and H. Liu, Potential Application of Metal Dichalcogenides Double-Layered Heterostructures as Anode Materials for Li-Ion Batteries, *J. Phys. Chem. C*, 2016, **120**, 4779–4788.

19 J. Hao, J. Zheng, F. Ling, Y. Chen, H. Jing, T. Zhou, L. Fang and M. Zhou, Strain-Engineered Two-Dimensional MoS$_2$ as Anode Material for Performance Enhancement of Li/Na-ion Batteries, *Sci. Rep.*, 2018, **8**, 2079.

20 D. Datta, J. Li, N. Koratkar and V. B. Shenoy, Enhanced Lithiation in Defective Graphene, *Carbon*, 2014, **80**, 305–310.

21 D. Datta, J. Li and V. B. Shenoy, Defective Graphene as a High-Capacity Anode Material for Na- and Ca-Ion Batteries, *ACS Appl. Mater. Interfaces*, 2014, **6**, 1788–1795.

22 X. Sun, Z. Wang and Y. Q. Fu, Defect-Mediated Lithium Adsorption and Diffusion on Monolayer Molybdenum Disulfide, *Sci. Rep.*, 2015, **5**, 18712.

23 K. Yao, Z. Xu, J. Huang, M. Ma, L. Fu, X. Shen, J. Li and M. Fu, Bundled Defect-Rich MoS$_2$ for a High-Rate and Long-Life Sodium-Ion Battery: Achieving 3D Diffusion of Sodium Ion by Vacancies to Improve Kinetics, *Small*, 2019, **15**, 1805405.

24 D. Ferguson, D. J. Searles and M. Hankel, Biphenylene and Phagraphene as Lithium Ion Battery Anode Materials, *ACS Appl. Mater. Interfaces*, 2017, **9**, 20577–20584.

25 Z. Wang, X.-F. Zhou, X. Zhang, Q. Zhu, H. Dong, M. Zhao and A. R. Oganov, Phagraphene: A Low-Energy Graphene Allotrope Composed of 5–6–7 Carbon Rings with Distorted Dirac Cones, *Nano Lett.*, 2015, **15**, 6182–6186.

26 B. Jang, J. Koo, M. Park, H. Lee, J. Nam, Y. Kwon and H. Lee, Graphdiyne as A High-Capacity Lithium Ion Battery Anode Material, *Appl. Phys. Lett.*, 2013, **103**, 263904.

27 H. Shang, Z. Zuo, L. Yu, F. Wang, F. He and Y. Li, Low-Temperature Growth of All-Carbon Graphdiyne on a Silicon Anode for High-Performance Lithium-Ion Batteries, *Adv. Mater.*, 2018, **30**, 1801459.

28 S. Najmaei, Z. Liu, W. Zhou, X. Zou, G. Shi, S. Lei, B. I. Yakobson, J.-C. Idrobo, P. M. Ajayan and J. Lou, Vapour Phase Growth and Grain Boundary Structure of Molybdenum Disulphide Atomic Layers, *Nat. Mater.*, 2013, **12**, 754–759.

29 A. M. van der Zande, P. Y. Huang, D. A. Chenet, T. C. Berkelbach, Y. You, G.-H. Lee, T. F. Heinz, D. R. Reichman, D. A. Muller and J. C. Hone, Grains and Grain Boundaries in Highly Crystalline Monolayer Molybdenum Disulphide, *Nat. Mater.*, 2013, **12**, 554–561.

30 Z. Zhang, X. Zou, V. H. Crespi and B. I. Yakobson, Intrinsic Magnetism of Grain Boundaries in Two-Dimensional Metal Dichalcogenides, *ACS Nano*, 2013, **7**, 10475–10481.

31 G. Barik and S. Pal, 2D Square Octagonal Molybdenum Disulfide: An Effective Anode Material for LIB/SIB Applications, *Adv. Theory Simul.*, 2020, **3**, 2000157.

32 Y. C. Cheng, Z. Y. Zhu, M. Tahir and U. Schwingenschlögl, Spin-Orbit–Induced Spin Splittings in Polar Transition Metal Dichalcogenide Monolayers, *Europhys. Lett.*, 2013, **102**, 57001.

33 J. Zhang, S. Jia, I. Kholmanov, L. Dong, D. Er, W. Chen, H. Guo, Z. Jin, V. B. Shenoy, L. Shi and J. Lou, Janus Monolayer Transition-Metal Dichalcogenides, *ACS Nano*, 2017, **11**, 8192–8198.

34 A.-Y. Lu, H. Zhu, J. Xiao, C.-P. Chuu, Y. Han, M.-H. Chiu, C.-C. Cheng, C.-W. Yang, K.-H. Wei, Y. Yang, Y. Wang, D. Sokaras, D. Nordlund, P. Yang, D. A. Muller, M.-Y. Chou, X. Zhang and L.-J. Li, Janus Monolayers of Transition Metal Dichalcogenides, *Nat. Nanotechnol.*, 2017, **12**, 744–749.

35 C. Shang, X. Lei, B. Hou, M. Wu, B. Xu, G. Liu and C. Ouyang, Theoretical Prediction of Janus MoSSe as a Potential Anode Material for Lithium-Ion Batteries, *J. Phys. Chem. C*, 2018, **122**, 23899–23909.

36 Y. Zhang, H. Ye, Z. Yu, Y. Liu and Y. Li, First-Principles Study of Square Phase MX$_2$ and Janus MXY (M = Mo, W; X, Y = S, Se, Te) Transition Metal Dichalcogenide Monolayers under Biaxial Strain, *Phys. E*, 2019, **110**, 134–139.

37 X. Lai, Y. Zhang, Y. Zheng, X. Xiang, H. Ye, W. Liu and Y. Liu, Catalytic Activity for Hydrogen Evolution Reaction in Square Phase Janus MoSSe Monolayer: A First-Principles Study, *Phys. E*, 2021, **126**, 114485.

38 Z. Wang, 2H → 1T′ Phase Transformation in Janus Monolayer MoSSe and MoSTe: An Efficient Hole Injection Contact for 2H-MoS$_2$, *J. Mater. Chem. C*, 2018, **6**, 13000–13005.

39 G. Kresse and J. Furthmüller, Efficient Iterative Schemes for Ab Initio Total-Energy Calculations Using A Plane-Wave Basis Set, *Phys. Rev. B: Condens. Matter Mater. Phys.*, 1996, **54**, 11169–11186.

40 P. E. Blöchl, Projector Augmented-Wave Method, *Phys. Rev. B: Condens. Matter Mater. Phys.*, 1994, **50**, 17953–17979.

41 J. P. Perdew, K. Burke and M. Ernzerhof, Generalized Gradient Approximation Made Simple, *Phys. Rev. Lett.*, 1996, **77**, 3865–3868.

42 H. J. Monkhorst and J. D. Pack, Special Points for Brillouin-zone Integrations, *Phys. Rev. B: Solid State*, 1976, **13**, 5188–5192.

43 S. Grimme, J. Antony, S. Ehrlich and H. Krieg, A Consistent and Accurate Ab Initio Parametrization of Density Functional Dispersion Correction (DFT-D) for the 94 Elements H-Pu, *J. Chem. Phys.*, 2010, **132**, 154104.

44 D. L. Cooper, J. Gerratt and M. Raimondi, Applications of Spin-Coupled Valence Bond Theory, *Chem. Rev.*, 1991, **91**, 929–964.

45 G. Henkelman, A. Arnaldsson and H. Jónsson, A Fast and Robust Algorithm for Bader Decomposition of Charge Density, *Comput. Mater. Sci.*, 2006, **36**, 354–360.

46 G. Henkelman, B. P. Uberuaga and H. Jónsson, A Climbing Image Nudged Elastic Band Method for Finding Saddle

Points and Minimum Energy Paths, *J. Chem. Phys.*, 2000, **113**, 9901–9904.

47 D. Alfè, PHON: A Program to Calculate Phonons Using the Small Displacement Method, *Comput. Phys. Commun.*, 2009, **180**, 2622–2633.

48 M. K. Aydinol, A. F. Kohan, G. Ceder, K. Cho and J. Joannopoulos, Ab Initio Study of Lithium Intercalation in Metal Oxides and Metal Dichalcogenides, *Phys. Rev. B: Condens. Matter Mater. Phys.*, 1997, **56**, 1354–1365.

49 C. Ataca, H. Şahin and S. Ciraci, Stable, Single-Layer MX$_2$ Transition-Metal Oxides and Dichalcogenides in a Honeycomb-Like Structure, *J. Phys. Chem. C*, 2012, **116**, 8983–8999.

50 Y. Ma, L. Kou, X. Li, Y. Dai, S. C. Smith and T. Heine, Quantum Spin Hall Effect and Topological Phase Transition in Two-Dimensional Square Transition-Metal Dichalcogenides, *Phys. Rev. B: Condens. Matter Mater. Phys.*, 2015, **92**, 085427.

51 Z. Wang and G. Shao, High-Capacity Cathodes for Magnesium Lithium Chlorine Tri-Ion Batteries through

Chloride Intercalation in Layered MoS$_2$: A Computational Study, *J. Mater. Chem. A*, 2018, **6**, 6830–6839.

52 Z. Li, X. Mu, Z. Zhao-Karger, T. Diemant, R. J. Behm, C. Kübel and M. Fichtner, Fast Kinetics of Multivalent Intercalation Chemistry Enabled by Solvated Magnesium-Ions into Self-Established Metallic Layered Materials, *Nat. Commun.*, 2018, **9**, 5115.

53 Y. Cheng, A. Nie, Q. Zhang, L.-Y. Gan, R. Shahbazian-Yassar and U. Schwingenschlogl, Origin of the Phase Transition in Lithiated Molybdenum Disulfide, *ACS Nano*, 2014, **8**, 11447–11453.

54 M. Mortazavi, C. Wang, J. Deng, V. B. Shenoy and N. V. Medhekar, Ab Initio Characterization of Layered MoS$_2$ as Anode for Sodium-Ion Batteries, *J. Power Sources*, 2014, **268**, 279–286.

55 Q. Huang, X. Li, M. Sun, L. Zhang, C. Song, L. Zhu, P. Chen, Z. Xu, W. Wang and X. Bai, The Mechanistic Insights into the 2H-1T Phase Transition of MoS$_2$ upon Alkali Metal Intercalation: From the Study of Dynamic Sodiation Processes of MoS$_2$ Nanosheets, *Adv. Mater. Interfaces*, 2017, **4**, 1700171.